Green Chemistry

ARTICLE

Photo-assisted water oxidation by high-nuclearity cobalt-oxo cores: tracing the catalyst fate during oxygen evolution turnover

Received 00th January 20xx,
Accepted 00th January 20xx

DOI: 10.1039/x0xx00000x

www.rsc.org/

M. Natali,[a] I. Bazzan,[b] S. Goberna-Ferrón,[c] R. Al-Oweini,[b,d] M. Ibrahim,[d] B. S. Bassil,[d] H. Dau,[e] F. Scandola,[a] J. R. Galán-Mascarós,[c] U. Kortz,[d] A. Sartorel,[b] I. Zaharieva,[e] and M. Bonchio[b,*]

Multi-nuclear cobalt cores have been proposed as the molecular analogs of the Natural Oxygen Evolving Complex, enabling water oxidation for artificial photosynthesis schemes and the production of solar fuels. In particular, Cobalt-substituted polyoxometalates (Co-POMs) display a record activity as water oxidation catalysts (WOC) in terms of turnover number, turnover frequency, and quantum yield, when combined in a light activated oxygen evolving cycle with $Ru(bpy)_3^{2+}$ (bpy = 2,2'-bipyridine) as the photosensitizer. The unique behavior of high-nuclearity cobalt clusters is addressed herein by employing Co-POMs with Co≥ 9 as molecular WOCs. The temporal dissection of the catalytic events is framed herein to investigate the initial photo-induced electron transfer (ET) occurring in the micro-to-millisecond time domain, and followed by the oxygen evolution kinetics taking place within a minute-to-hours regime. In particular, flash photolysis shows ET from the Co-POM to photogenerated $Ru(bpy)_3^{3+}$ with well behaved, diffusional, kinetics (bimolecular rate constants in the range k_{ET}= 2.1 - 5.0 × 10^9 $M^{-1}s^{-1}$) and counting up to 32 ET events in a 60 ms timeframe. The evolution of Co-POMs is then traced under oxygenic conditions, where infrared and X-ray absorption spectroscopy (XAS) indicate that POM based structures are competent catalysts under photo-assisted turnover regime.

Introduction

Solar water splitting into O_2 and H_2, has the potential to solve the renewable energy impasse, albeit posing one formidable chemical challenge, i.e. the multi-electron oxidation of water which is still the crucial bottleneck of the overall process.[1] The long-sought goal is the discovery of a cost-effective water oxidation catalyst (WOC)[2] enabling O_2 evolution using visible light irradiation while offering multi-turnover performance, long term stability, and a sustainable, wide distribution and availability implemented by the use of "earth-abundant" transition metals.

Indeed, Nature has evolved a unique tetra-manganese cluster, embedded in photosystem II enzymes (PSII), that is responsible for photo-induced water oxidation and provides the chemical engine of all photosynthetic organisms.[3] Therefore, synthetic WOCs have been conceived along bio-inspired guidelines, by a tailored design of multi-redox transition metal manifolds that can oxidize water and evolve oxygen via a stepwise, light-activated, mechanism. While the complexity of the photo-assisted mechanism depends on the catalytic routine and is hardly described by one single scenario, two key events are typically comprised at the start and closing of the oxygen evolution cycle:

(i) a luminous phase taking place, by a sequence of photo-induced electron transfer (ET) events, through which the catalyst reaches a high-valent (oxidized), reactive state, upon multi-"hole" accumulation;

(ii) a dark phase of oxygen release, which restores the catalyst in its resting (reduced) state, and guarantees catalytic turnover.

Photo-induced ET is expected to take place in the first steps of the catalytic regime by ultra-fast events, occurring in the

[a] Department of Chemical and Pharmaceutical Sciences, University of Ferrara, Via Fossato di Mortara 17-19, and Centro Interuniversitario per la Conversione Chimica dell'Energia Solare (SolarChem), sez. di Ferrara, via L. Borsari 46, 44121 Ferrara, Italy.
[b] Department of Chemical Sciences University of Padova and Institute on Membrane Technology, Unit of Padova, via F. Marzolo 1, 35131, Padova, Italy.
[c] Institute of Chemical Research of Catalonia (ICIQ), The Barcelona Institute of Science and Technology (BIST), Av. Paisos Catalans, 16, E-43007, Tarragona (Spain) and ICREA, Passeig Lluis Companys, 23, E-08010, Barcelona (Spain).
[d] Jacobs University, Department of Life Sciences and Chemistry, Campus Ring 1, 28759 Bremen (Germany).
[e] Freie Universität Berlin, FB Physik, Arnimallee 14, 14195 Berlin, Germany.

Current addresses:
IB Institut Lavoisier de Versailles, UMR 8180, Université Paris-Saclay, Université de Versailles Saint-Quentin en Yvelines, 45 Avenue des Etats-Unis, 78035 Versailles cedex, France
SGF ESRF — The European Synchrotron, 71 Avenue des Martyrs, 38000 Grenoble, France.
RAO Department of Chemistry, Faculty of Science, Beirut Arab University P.O. Box 11 50 20, Riad El Solh 1107 2809 Beirut, Lebanon
MI Institute of Nanotechnology, Karlsruhe Institute of Technology (KIT), Hermann-von-Helmholtz Platz 1, 76344 Eggenstein-Leopoldshafen, Germany
BSB Department of Chemistry, Faculty of Sciences, University of Balamand, P. O. Box 100, Tripoli, Lebanon

Electronic Supplementary Information (ESI) available: Conductometric titrations, pulsed emission experiments, laser flash photolysis, UV-vis analysis of reaction mixtures, infrared spectroscopy, EXAFS spectroscopy. See DOI: 10.1039/x0xx00000x

micro-to-milliseconds time domain. On the contrary, the dark chemical transformations dictate the slow oxygen evolution kinetics and turnover frequency (TOF), spanning from a second-to-hour temporal window.

The photocatalytic system is thus exposed to alternating light-induced/dark-phase phenomena, where stability and/or structural dynamics regulate the overall turnover performance. Modification of the catalyst structure during turnover regime, and spanning diverse time-boundaries, is indeed one major issue of solar water splitting in both natural and artificial systems. Aiming at the WOC up-grade, the identification of the competent species, generated from the catalyst initial state, is instrumental to draw any possible structure-reactivity relationships. In this quest polyoxometalates (POMs) have been proposed as the structural analogues of the natural PSII cluster, thus providing a functional model of the photoactivated cycle *in-vitro*.[4-6]

POMs are a versatile family of catalysts exhibiting a nano-dimensional but molecular metal-oxide structure, that can be tuned to integrate multi-nuclear WOC cores.[4,5] Cobalt-substituted POMs are among the most promising ones[6] vis-à-vis the imperative goal of a sustainable energy economy and "green" catalysis avoiding the use of rare and expensive noble-metals. Moreover, the toxicity of Co-POMs has been addressed in aqueous solution and depends on the concentration conditions and the time of exposure, as demonstrated in the case of $[Co_4(H_2O)_2(PW_9O_{34})_2]^{10-}$.[6b] Noteworthy, its encapsulation into a carboxymethyl chitosan matrix is instrumental to override the toxicity effects.[6b] This observation highlights the key importance of a tailored material choice for the up-grade to energy devices.[7]

The POM structure is shaped to encapsulate a discrete cobalt-oxide fragment, so as to provide a molecular equivalent of amorphous cobalt oxide phases,[8,9] albeit with an improved stability in water, featuring a highly hydrophilic and electron-withdrawing POM environment. Several POM-based platforms have been described to incorporate cobalt WOCs, with formula:

$[CoMo_6O_{24}H_6]^{3-}$ and $[Co_2Mo_{10}O_{38}H_4]^{6-}$,[10]

$[Co(H_2O)(CoW_{11}O_{39})]^{7-}$,[11]

$[Co_4(H_2O)_2(PW_9O_{34})_2]^{10-}$, $[Co_4(H_2O)_2(VW_9O_{34})_2]^{10-}$,[12-16]

$[\{Co_4(\mu\text{-}OH)(H_2O)_3\}(Si_2W_{19}O_{70})]^{11-}$,[17]

$[Co_4(H_2O)_2(SiW_9O_{34})_2]^{12-}$,[18]

$[Co_9(H_2O)_6(OH)_3(PW_9O_{34})_3]^{16-}$,[19]

$[\{Co_4(OH)_3(PO_4)\}_4(XW_9O_{34})_4]^{n-}$ (X=Si, Ge, n=32 ; X = P, As, n =28).[20] Among them, cobalt oxide clusters with high nuclearity have shown an increased stability at neutral pH, and could be dispersed within a solid state matrix.[21] Thus, they are particularly promising for their implementation into functional water photo-splitting schemes. In this case, the POM based WOC is generally used in combination with $Ru(bpy)_3^{2+}$ (bpy = 2,2'-bipyridine) as the photosensitizer and in the presence of sodium persulfate, $S_2O_8^{2-}$ as sacrificial electron acceptor, giving rise to a cascade of events spanning a time sequence from nano-seconds to hours, as described by equations 1-6.[5]

Photogeneration of $Ru(bpy)_3^{3+}$ as oxidant (nanoseconds)

$Ru(bpy)_3^{2+} + h\nu \rightarrow {}^*Ru(bpy)_3^{2+}$ (1)

${}^*Ru(bpy)_3^{2+} + S_2O_8^{2-} \rightarrow Ru(bpy)_3^{3+} + SO_4^{2-} + SO_4^{\cdot-}$ (2)

$Ru(bpy)_3^{2+} + SO_4^{\cdot-} \rightarrow Ru(bpy)_3^{3+} + SO_4^{2-}$ (3)

Hole accumulation by ET from WOC to $Ru(bpy)_3^{3+}$ (micro-to-milli-seconds)

$Ru(bpy)_3^{3+} + WOC \rightarrow Ru(bpy)_3^{2+} + WOC^{+}$ (4)

$n\ Ru(bpy)_3^{3+} + WOC \rightarrow n\ Ru(bpy)_3^{2+} + WOC^{n+}$ (5)

Water oxidation and oxygen evolution (minutes-to-hours)

$WOC^{n+} + 2\ H_2O \rightarrow WOC^{(n-4)+} + O_2 + 4\ H^{+}$ (6)

Within these reaction schemes, the POM activity is readily assessed on the basis of the primary photo-induced ET events, leading to WOC oxidation (equations 4-5). In this view, laser flash photolysis studies, monitoring photoinduced ET from the POM donor, have been proposed as functional probe to evaluate the POM behaviour in the micro-second time domain and sorting out initial decomposition issues.[5,22-24] For instance, diffusional ET occurring within a bimolecular POM-sensitizer, donor-acceptor interaction (k_{ET} = 3.6×10^9 $M^{-1}s^{-1}$), has been observed for a tetraruthenium polyoxotungstate, namely $\{Ru_4O_4(\mu\text{-}OH)_2(H_2O)_4[\gamma\text{-}SiW_{10}O_{36}]\}^{10-}$.[22]

Herein we compare and contrast the activity of $[Co_9(H_2O)_6(OH)_3(PW_9O_{34})_3]^{16-}$ (**Co_9**),[25] $[Co_6(H_2O)_{30}\{Co_9Cl_2(OH)_3(H_2O)_9(SiW_8O_{31})_3\}]^{5-}$ (**Co_{15}**)[26] and $[\{Co_4(OH)_3PO_4\}_4(PW_9O_{34})_4]^{28-}$ (**Co_{16}**)[27] (Figure 1) along a photocatalytic cycle with $Ru(bpy)_3^{2+}$ ultimately evolving oxygen from water (eqns 1-6). Our results include the dissection of the light-phase, by investigating the photo-induced ET kinetics from few μs to tens of ms, and the following dark-catalysis from minutes to several hours when oxygen evolution is observed.

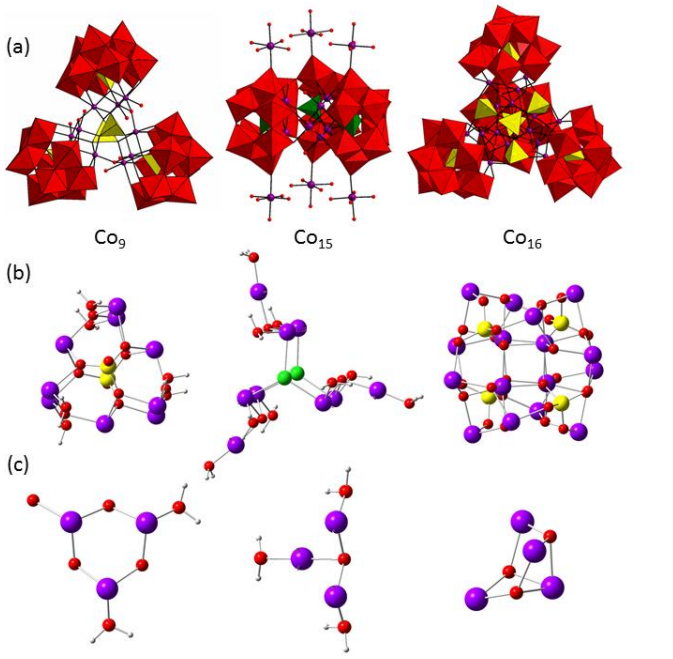

Figure 1. Combined polyhedral/ball and stick representation of (a) **Co_9**, **Co_{15}**, **Co_{16}** POMs (b) the corresponding multi-cobalt cores and (c) cobalt core building-block. Color code: WO_6 octahedra in red, PO_4 tetrahedra in yellow, SiO_4 tetrahedra in green; P atoms in yellow, Co atoms in violet, Cl atoms in green, O atoms in red, H atoms in white (not shown in μ-OH bridges for clarity reasons).

In particular, we highlight the key role of the polyoxotugstate platform, binding the cobalt-oxo domains, to leverage fast and multiple electron transfer to photogenerated $[Ru(bpy)_3]^{3+}$ (equations 4-5). Optimization of the light-to-catalyst interface is one key target to enhance the photo-conversion efficiency towards sustainable energy schemes. The POM-based innovation can exploit a favorable interplay of electrostatic association forces and hydrogen-bonded network, that cooperate in the self-assembly of the photosynthetic unit. This is one key point of advancement with respect to the vast literature on covalently linked dyads,[28] generally affected by major recombination pathways and therefore unable to exploit the charge-separation state for any significant catalytic transformation. Our results set an informative structural-reactivity study on high nuclearity, Co-oxo phases (number of Co atoms ≥ 9), confined by rigid and highly hydrophilic POM cages, which impart a definite, nano-topology of the catalytic site. Noteworthy, the molecular nature of the POM catalytic core allows for a precise mapping of its evolution under photo-assisted water oxidation, as probed herein by X-ray Absorption Spectroscopy (XAS).

Results and discussion

Structural features of Co-POMs. As a common feature, these polyanions display a discrete multi-nuclear Co(II) core, where the metal ions are connected by bridging ligands, namely oxo, hydroxo, hydrogenophosphato, phosphato and/or chloro ligands (Figure 1 and Table 1). Oxygen evolving cores, with related structure, have been identified as the reactive sites of cobalt (II,III) oxides, that retain a high appeal and are among the state-of-the-art catalysts for water oxidation.[8,9,29-30] For these latter, only 1% of cobalt sites within the bulk material accounts for the observed WOC activity, which turns out to be highly sensitive to surface modifications and structural defects.[30] In particular a di-nuclear $\{Co_2O_2\}$ unit has been identified as the minimal functional building block of the cobalt core, including $\{Co_4O_6\}$ cubanes or extended polymers.[29] As a general feature, a high degree of oxygen vacancy, and therefore the availability of water coordination sites, turns out to be a key effector for the WOC performance.[30] Indeed, when the redox-active metal site is associated to terminal aqua or hydroxo ligands, the occurrence of proton-coupled electron transfer (PCET) events favors the formation of high-valent metal-oxo intermediates by low-energy pathways, being at the turning point for the efficient use of visible light irradiation, fast turnover frequency and long-term operation stability.

Table 1 collects the main structural features of the cobalt cores and of surface sites, ascribed to the selected Co-POMs under investigation (Figure 1), highlighting the minimal cluster composition (triads or cubanes of connected cobalt ions), their bridging units, the presence of "outer-core" cobalt sites, and the number of terminal aqua-ligands as a direct probe of the WOC open coordination sites.

In particular:

- **Co_9** displays a cobalt core, with formula $\{Co_9(\mu\text{-}OH)_3(H_2O)_6(HPO_4)_2\}$, composed of three $\{Co_3(\mu\text{-}OH)_3(H_2O)_6\}$ triads connected through two HPO_4^{2-} bridges, with a triangle of triangles arrangement, and six terminal water molecules.
- **Co_{15}** displays a cobalt core, with formula $\{Co_9(\mu\text{-}OH)_3(H_2O)_9Cl_2\}$, composed of three $\{Co_3(\mu\text{-}OH)(H_2O)_3\}$ triads connected through two Cl^- bridges, and six "outer-core" satellite $Co(H_2O)_5$ groups, bound to terminal oxo groups of the POM surface.[26]‡ In **Co_{15},** a total of 39 terminal water ligands are bound to cobalt centres , 9 to the nonanuclear core, and 30 to the satellite cobalt atoms).
- **Co_{16}** displays a cobalt core, with formula $\{Co_{16}(\mu\text{-}OH)_{12}(PO_4)_4\}$, composed of four $\{Co_4(\mu\text{-}OH)_3\}$ distorted cubanes connected through the four phosphate moieties.[20,27],§ No water molecules are found as terminal ligands of the Cobalt core, so that its WOC performance has to be ascribed to substitution equilibria likely involving the phosphate groups.[20]

Table 1. Structural features of POM-embedded multi-cobalt cores under investigation (see Figure 1).

Co-POM (charge)	Description of cobalt core	Bridging ligands	terminal waters
Co_9 (16-)	**three** $\{Co_3(\mu\text{-}OH)_3(H_2O)_2\}$ **triads**	3 OH^-, 2 HPO_4^{2-}	6
Co_{15} (5-)	**three** $\{Co_3(\mu\text{-}OH)(H_2O)_3\}$ **triads**	2 Cl^-, 3 OH^-	9
Co_{16} (28-)	**four** $\{Co_4(\mu\text{-}OH)_3\}$ distorted **cubanes**	12 OH^- , 4 PO_4^{3-}	-

These Co-POMs are soluble in aqueous solution where their molecular structure is maintained as confirmed by convergent techniques.[19-21,25-27] In particular, solution equilibria likely involving the leaching of paramagnetic Co(II) aqua ions have been addressed by means of ^{31}P-NMR line broadening analysis[31] under the conditions employed for the photocatalytic studies (20 mM phosphate buffer, pH 8, figure S1). In these experiments, the full width at half maximum (FWHM) registered for the ^{31}P NMR signal of the phosphate buffer provides a direct estimate of the Co(II) aquo-ions concentration, calibrated in the range 0 – 12.5 μM (figure S1). In particular, for [**Co_{15}**]= 17 μM, a [Co(II)]= 16 ± 1 μM is estimated as the upper limit of cobalt leaching,‡‡ corresponding to the release of one satellite cobalt center, and to a maximum of ca 6% leaching of the total cobalt amount. Under analogous conditions, the cobalt leaching of **Co_9** and **Co_{16}** falls below the analysis detection limit, being detected only at higher Co-POM concentration, where [**Co_9**]= 110 μM yields [Co(II)]= 11 ± 0.6 μM and [**Co_{16}**]= 62 μM yields [Co(II)]< 1 μM, corresponding respectively to 1% and <0.1% leaching of the total cobalt amount.

$Ru(bpy)_3^{2+}$ / Co-POMs ion pairs. The polyanionic nature of polyoxometalates has important implications for association

equilibria involving cationic photosensitizers. Formation of ion pairs is responsible for direct quenching of the photosensitizer excited state by the associated POM[5,22-24,32,33], resulting in a major decrease of the photosensitizer emission, thus competing with the oxidant photogeneration step (eq. 2).[5,22b,32] Conductometric titrations show the formation of ion pairs between $Ru(bpy)_3^{2+}$ and the Co-POMs under investigation in water (Figures S2-S4 in Supporting Information). In all cases, the equivalence point corresponds to the expected charge balance ratio, $(Ru(bpy)_3^{2+}$/Co-POM = 1:8, 1:2.5 and 1:14, respectively for **Co_9**, **Co_{15}** and **Co_{16}**. The impact of ion pair formation on the photosensitizer emission has been verified by fluorencence quenching experiments (Figure 2). Indeed, $Ru(bpy)_3^{2+}$ emission (50 μM in water) is remarkably abated upon addition of equimolar Co-POMs (compare black and red traces in Figure 2). The residual emission (see, e.g., red traces in Figure 2a,c) is also appreciably red-shifted (ca 10 nm) in the presence of the Co-POM, thus suggesting a substantial electronic interaction between the $Ru(bpy)_3^{2+}$ sensitizer and the Co-POM, which further confirms the occurrence of ion-pair equilibria. Pulsed emission experiments show that the $Ru(bpy)_3^{2+}$ excited state has a constant lifetime, and confirm the occurrence of static quenching within ion pairs (Figure S5 in Supporting Information). Interestingly, the decrease of $Ru(bpy)_3^{2+}$ emission, induced by Co-POMs, is observed in the range **Co_{16}** (70% abatement) > **Co_9** (55%) > **Co_{15}** (10%) and reflects the overall negative charge of the polyanion as the main driving force for the ion pair association. Indeed, buffering of the ionic strength by addition of sodium sulfate (5-50 mM) to $Ru(bpy)_3^{2+}$/**Co_{16}** and $Ru(bpy)_3^{2+}$/**Co_9** solutions, leads in both cases to >85% recovery of the photosensitizer emission and to the concomitant blue-shift of the luminescence maxima (green, blue and orange traces in Fig. 2a,c). Noteworthy, the use of a 50 mM phosphate buffer (pH 8) favors a loose $Ru(bpy)_3^{2+}$/Co-POMs electrostatic interaction, which maintains the $Ru(bpy)_3^{2+}$ emission under photo-assisted catalysis (Figure S6 in Supporting Information). This is instrumental in preventing a competitive quenching of the $Ru(bpy)_3^{2+}$ excited state by Co-POMs as alternative to the primary oxidative step with $S_2O_8^{2-}$ (eqns. 1-3 of the photo-assisted catalytic cycle).

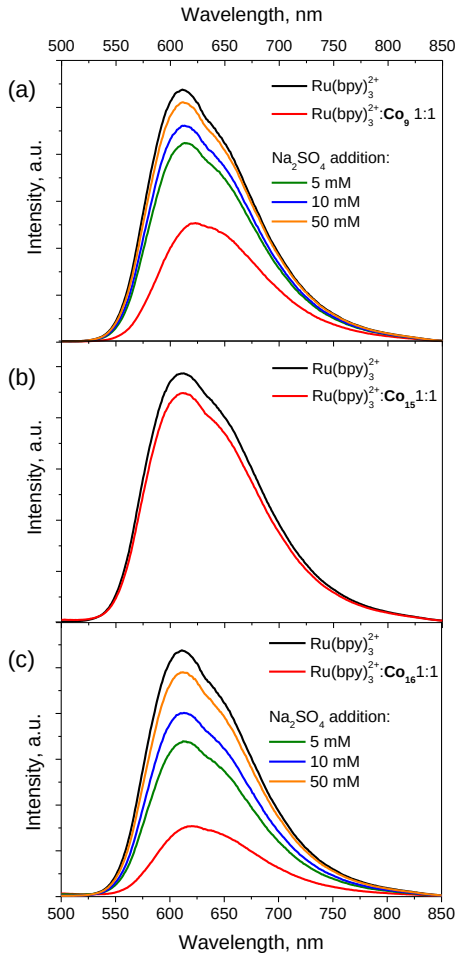

Figure 2. Variation of $Ru(bpy)_3^{2+}$ photoluminescence (50 μM, air-equilibrated water solution, excitation at 450 nm) upon addition of **Co_9** (a) **Co_{15}** (b) and **Co_{16}** (c). Black traces: $Ru(bpy)_3^{2+}$ (reference); red traces: $Ru(bpy)_3^{2+}$:Co-POM 1:1; green, blue, orange traces: $Ru(bpy)_3^{2+}$:Co-POM 1:1 in the presence of 5-50 mM Na_2SO_4.

Hole scavenging events and kinetics. According to the persulfate sacrificial cycle, photogeneration of $Ru(bpy)_3^{3+}$ occurs by direct oxidative quenching of the $Ru(bpy)_3^{2+}$ excited state, and by a dark reaction of its ground state with a photo-generated sulfate radical (eqns 1-3). Under these conditions, the maximum value of quantum yield is 2 as two molecules of $Ru(bpy)_3^{3+}$ are possibly generated upon absorption of one photon.[5,34] Photogeneration of $Ru(bpy)_3^{3+}$ is confirmed by the ultra-fast bleaching of the $Ru(bpy)_3^{2+}$ ground state (λ = 450 nm), registered under laser flash photolysis conditions (Figure 3). These studies are of particular interest as they provide a direct evidence of the multi-hole scavenging occurring in the presence of the selected Co-POM (oxidation of the Co-POM by photogenerated $Ru(bpy)_3^{3+}$, eqns 4-5). The key information is twofold: (i) the kinetics of the primary hole-scavenging event, occurring by photo-induced ET from the Co-POM donor; (ii) the number of hole-scavenging events, corresponding to the number of electrons removed from the Co-POM donor, and stimulated by photo-irradiation in a millisecond temporal window. The rate of the primary *hole scavenging* event under

photoirradiation conditions (eqn 4) ranks the potential WOCs, in terms of slow or fast donors with respect to $Ru(bpy)_3^{3+}$. Slow hole scavenging WOCs (millisecond time scale) are responsible for the accumulation of $Ru(bpy)_3^{3+}$ and for its irreversible oxidative degradation, as in the case of Ir-oxide colloids.[35] POM-based WOCs provide the fastest hole scavenging processes known up-to-date (microsecond time scale), showing well-behaved kinetics and multiple electron transfer efficiency.[5,22-24]

Nanosecond flash photolysis was used to probe the high nuclearity cobalt POMs under photo-induced ET conditions, upon generation of $Ru(bpy)_3^{3+}$ with sodium persulfate, and by monitoring the $Ru(bpy)_3^{2+}$ bleach recovery over time, (recovery of the metal-to-ligand-charge-transfer absorption, MLCT, at λ_{max} 450 nm) in a relatively wide window (0–60 ms).[§§]

Flash photolysis (excitation at λ_{max} 355 nm, 8 ns pulses) of $Ru(bpy)_3^{2+}$ (50 μM) and $Na_2S_2O_8$ (5 mM) in aqueous phosphate buffer, pH 8, shows a fast bleach (negative ΔOD, black trace in Fig. 3) persisting in the timescale of the experiment of 200 μs, and indicative of the $Ru(bpy)_3^{3+}$ photogeneration. Bleach recovery, associated to its back reduction to $Ru(bpy)_3^{2+}$, is obtained upon addition of increasing concentrations of the Co-POM. Representative kinetics are shown for **Co_9** in Fig. 3 (see Fig. S7 in Supporting Information for **Co_{15}** and **Co_{16}** kinetics). Under pseudo-first-order conditions (excess **Co_9** over photogenerated $Ru(bpy)_3^{3+}$), fitting of the recovery traces yields bimolecular rate constants which are associated to primary hole scavenging event by the WOC (eq. 4). For the Co-POMs under investigation, the resulting second order rate constants are exceptionally high, within one order of magnitude of diffusion-controlled rates, with values of 2.1±0.3 $\times10^9$, 5.0±0.4 $\times10^9$, 4.5±0.4 $\times10^9$ $M^{-1}s^{-1}$ respectively found for **Co_9**, **Co_{15}** and **Co_{16}** (Fig. 3b and table 2). These kinetic rate constants are roughly proportional to the number of Cobalt atoms of the Co-POMs, suggesting that the electron transfer to $Ru(bpy)_3^{3+}$ originates from the Co(II) atoms evolving to Co(III), and occurring with favorable thermodynamic driving force. This is confirmed by cyclic and square-wave voltammetry (Fig. S8 and S9, respectively) of the Co-POMs showing the anodic processes relative to the $Co^{III/II}$ couples in the potential range E ~ 0.80-1.00 V vs Ag/AgCl (for $Ru(bpy)_3^{3+/2+}$ E= 1.06 V vs Ag/AgCl).[‖] Moreover, the hole-scavenging rate is not changed, and remains constant, even after aging of the Co-POM solutions up to three hours. This behavior is very different from what observed for the parent $[Co_4(H_2O)_2(PW_9O_{34})_2]^{10-}$, where a steady increase of the photo-induced ET rate occurs over time, in a timescale of 90 minutes, thus indicating the conversion of the WOC to a more reactive ET donor over time.[14]

In this case, the constant value of the ET kinetics speaks against a progressive leaching of Co(II) aqua ions, that would result in a major abatement of the ET rate, as Co(II) aqua ions are inert with respect to hole-scavenging in the experimental timeframe of observation.[14]

Multi-hole accumulation upon sequential ET under photo-irradiation (eq. 5), have been confirmed by flash photolysis studies using a sub-stoichiometric WOC solution, while monitoring the $Ru(bpy)_3^{2+}$ bleach recover in an extended time window of ca 60 ms (Fig. 4). In such timescale, and adjusting the Co-POM concentration in terms of the overall cobalt content (in a range 8-9 μM), **Co_9**, **Co_{15}** and **Co_{16}** were found to react with 7.5, 32 and 20 $Ru(bpy)_3^{3+}$ equivalents, respectively, corresponding to ca. 0.8 (for **Co_9**), 2.1 (for **Co_{15}**) and 1.2 (for **Co_{16}**) average oxidation steps per cobalt center.

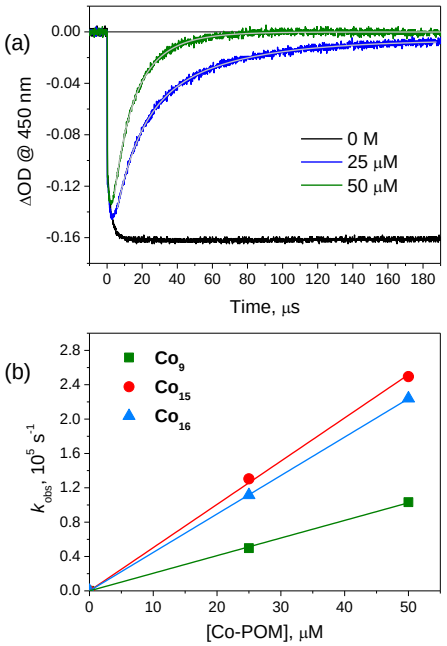

Figure 3. (a) Laser flash photolysis experiments (λ_{exc} = 355 nm) in aqueous phosphate buffer (pH 8) containing 5 mM $S_2O_8^{2-}$, 50 μM $Ru(bpy)_3^{2+}$, and 0-50 μM **Co_9**. (b) plots of pseudo-first-order rate constants of bleach recovery vs catalyst concentration, yielding bimolecular hole scavenging rate constants of 2.1×10^9, 5.0×10^9, 4.5×10^9 $M^{-1}s^{-1}$ for **Co_9**, **Co_{15}** and **Co_{16}**, respectively.

Noteworthy, while a one-electron oxidation of the cobalt-core is apparent for **Co_9** and **Co_{16}**, the peak value of 2.1 ET processes resulting for **Co_{15}**, indicates an overall Co(II) to Co(IV) redox change of the POM cobalt centers under photo-irradiation. The **Co_{15}** unique behavior, compared to the other high nuclearity Co-POMs, can be ascribed to its specific structural feature, with six satellite $Co^{II}(H_2O)_5$ groups grafted on the outer POM surface and a POM embedded cluster of three $\{Co_3(\mu\text{-}OH)(H_2O)_3\}$ triads (Figure 1). In this asset, the POM scaffold is expected to boost ET kinetics of the grafted Co(II) aqua ions as well as of the inner core.[11][¶] Moreover, **Co_{15}** displays 39 terminal waters coordinated to the cobalt centers, that are a proof of the broad WOC accessibility and favors the multi-hole accumulation mechanism by proton-coupled electron transfers (PCET) step.[36] Co(IV)-oxo groups, that form upon two sequential PCET steps from Co(II)-aquo moieties, have been indicated as the competent oxygen evolution sites of cobalt oxide WOCs.[37] Therefore, fast generation of Co(IV) sites, as observed for **Co_{15}**, is expected to play a key role for WOC performance in terms of the oxygen evolution kinetics.

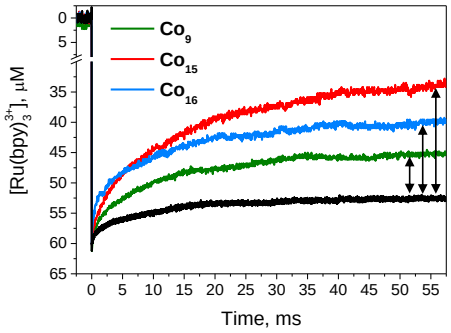

Figure 4. (a) Laser flash photolysis experiments (λ_{exc} = 355 nm) in aqueous phosphate buffer (pH 8) containing 5 mM $S_2O_8^{2-}$, 50 μM $Ru(bpy)_3^{2+}$ (black trace), and 1 μM **Co_9**. (green trace), 0.5 μM **Co_{15}** (red trace), and 0.5 μM **Co_{16}** (blue trace). The amount of $Ru(bpy)_3^{3+}$ reduced by the catalyst in the time lag of the experiment (indicated by vertical double arrows) is 7.5 μM for **Co_9**, 16 μM for **Co_{15}** and 10 μM for **Co_{16}**.

Table 2. Hole scavenging parameters of Co-POMs in aqueous phosphate buffer (pH 8), λ_{exc} = 355 nm containing 5 mM $S_2O_8^{2-}$, 50 μM $Ru(bpy)_3^{2+}$, and 0-100 μM Co-POMs.

Co-POM	$k^a/10^9$ $M^{-1}s^{-1}$	n(ET)[b]	redox steps
Co_9	2.1 ± 0.3	7.5	0.8
Co_{15}	5.0± 0.4	32	2.1
Co_{16}	4.5± 0.4	20	1.2

[a]Second order kinetic constant for primary hole scavenging of photo-generated $Ru(bpy)_3^{3+}$ by Co-POMs (λ_{exc} = 355 nm in aqueous phosphate buffer pH 8 containing 5 mM $S_2O_8^{2-}$, 50 μM $Ru(bpy)_3^{2+}$, and 0-100 μM Co-POM, see figures 3 and S6). [b]Number of photo-induced ET events calculated from bleach recovery occurring in 60 ms as $[Ru(bpy)_3^{2+}]$/[Co-POMs] (λ_{exc} = 355 nm in aqueous phosphate buffer pH 8 containing 5 mM $S_2O_8^{2-}$, 50 μM $Ru(bpy)_3^{2+}$, and Co-POM with a total Co concentration of 8-9 μM, see figure 4). [c]Average oxidation equivalents per cobalt center calculated as n(ET)/number of cobalt sites.

Oxygen evolving catalysis. Photo-assisted oxygen evolution by the Co-POMs under investigation has been addressed under turnover conditions within the $Ru(bpy)_3^{2+}/S_2O_8^{2-}$ sacrificial cycle, in 20 mM phosphate buffer, pH 8 (Table 3). In all cases, the oxygen evolution kinetics show a well behaved profile, with no induction period as oxygen production is registered in the immediate contingency of illumination, with a steep initial rate (R_0 calculated at <10% conversion), and levelling off to a plateau yield (up to 11 % persulfate conversion) after ca. 30-60 minutes of irradiation (Fig. S10 in Supporting Information). UV-Vis analysis of the spent reaction mixture (Figure S11 in Supporting Information) is consistent with an irreversible degradation of the ruthenium photosensitizer), which is thus responsible for the switching off of the photo-assisted catalysis.[5,22-24] Inspection of data in Table 3 points to address the Co-POM activity in terms of their photo-assisted WOC performance, by comparing the overall oxygen productivity and the initial oxygen evolution rate R_0 as a function of the POM concentration, and of the total Co loading (Table 3: [Co] = 19 - 147 μM, $[Ru(bpy)_3^{2+}]$ = 1 mM, $[S_2O_8^{2-}]$ = 5 mM).

Table 3. Photo-assisted oxygen production by Co-POMs within a $Ru(bpy)_3^{2+}/S_2O_8^{2-}$ sacrificial cycle.[a] Estimated errors from experiments run in duplicate: ±0.05 μmol O_2 in the total production of oxygen, and ± 0.1 μmol·s^{-1} for the $R_0\times10^3$.

#	Co-POM, μM ([Co], μM[b])	μmol O_2 (TON)[c]	$R_0\times10^3$,[d] μmol·s^{-1} (TOF×10^3, s^{-1})[e]
1	**Co_9**, 6.60 (58)	1.0 (10)	0.5 (5.0)
2	**Co_9**, 16.33 (147)	1.3 (5.3)	1.1 (4.5)
3	**Co_{15}**, 1.27 (19)	2.0 (105)	0.8 (42)
4	**Co_{15}**, 3.86 (58)	3.1 (53)	1.2 (21)
5[f]	**Co_{15}**, 9.80 (147)	4.1 (28)	2.8 (19)
6	**Co_{16}**, 3.62 (58)	2.0 (37)	1.3 (24)
7	**Co_{16}**, 9.19 (147)	3.9 (28)	3.0 (22)

[a] In all reactions: 15 ml of a 20 mM phosphate buffered solution (pH 8) containing $Ru(bpy)_3^{2+}$ (1 mM), $S_2O_8^{2-}$ (5 mM) and **Co_9**, **Co_{15}** or **Co_{16}**. Irradiation with a tungsten lamp (cut-off filter at 375 nm, power density 90 mW·cm^{-2}). [b] total cobalt concentration. [c] TON = turnover number defined as μmol O_2/μmol WOC, determined after 1 h irradiation, persulfate conversion yield is in the range 3-11%. [d] R_0 initial rate of O_2 production determined in the first 5 minutes of reaction. [e] TOF = turnover frequency defined as the maximum rate of O_2 production (expressed in μmol/s) over the μmol of WOC. [f] quantum yield = 0.055 with monochromatic LED illumination (λ=450 nm, photon flux = 2.63×10^{-8} einstein/s).

Under the conditions explored, the WOC performance follows the trend **Co_{15}** ~ **Co_{16}** > **Co_9** which turns out to be in line with the flash photolysis results (compare rate versus Cobalt concentration in Figure 3 and Figure S10). In particular, a linear dependence on the Co-POM concentration is observed both for the primary ET kinetics (up to 100 μM, Figure 3) and for the oxygen evolution kinetics (up to 10 μM, Figure S10). This observation is consistent with the molecular nature of the competent WOC, and speaks against any major structural leaching of Co(II) ions under the conditions adopted (see further discussion). The best performing **Co_{15}** displays a remarkable activity at a μM cobalt concentration (entry 3 in table 3, [**Co_{15}**] = 1.27 μM, total [Co] = 19 μM, 20 mM phosphate buffer pH 8), with turnover number, TON, up to 100, and a turnover frequency, TOF = 42 ×10^{-3} s^{-1}, in line with previous observations,[20] while the current literature benchmark, $[Co_4(H_2O)_2(VW_9O_{34})_2]^{10-}$, is reported to reach up to 4 s^{-1} in 80 mM borate buffer[16] (compare entry 3 and 2 in Table S3 in Supporting Information).[6,11-18,20]
The quantum yield[5] associated to oxygen production by **Co_{15}** under photoirradiation with monochromatic emitting LEDs (λ=450 nm, photon flux = 2.63×10^{-8} einstein/s) turns out to be ϕ = 0.055. This value has been determined at a higher catalyst concentration to maximize the rate and the amount of the evolved oxygen (entry 5 in Table 3, [**Co_{15}**] = 16.33 μM, [Co] = 147 μM, 20 mM phosphate buffer pH 8). Quantum yields associated to the use of cobalt substituted polyoxotungstates in $Ru(bpy)_3^{2+}/S_2O_8^{2-}$ sacrificial cycles have been reported in few cases, using diverse buffers, pH, and illumination sources, with values up to ϕ = 0.34 (Table S4). Our data provide a direct

comparison with Co(II) aquo-ions (ϕ = 0.11, λ=450 nm, photon flux = 1.58×10^{-7} einstein·s^{-1}, [Co] = 72 μM, borate buffer, pH 8,)[38] as it turns out that higher-nuclearity Co-POMs have a rather distinct behavior with respect to POM-based analogues and to what are generally invoked as a contamination impurities, Co^{2+} ions and cobalt-oxide nanoparticles (Table S4).

Tracing the fate of Co-POMs after oxygenic turnover. As part of the life-cycle analysis of the high nuclearity Co-POMs, we have addressed their possible structural modification during photoirradiation, after oxygen evolution.

To this aim, **Co_9**, **Co_{15}** and **Co_{16}** were recovered from the spent reaction mixtures (entries 2, 5, 7 in Table 3) by precipitation with $Ru(bpy)_3^{2+}$ added in excess.♣ In all cases, the FT-IR spectra of the isolated complexes show the expected absorption bands ascribed to a Co-POM species, where only modest wavenumber shifts are observed with respect to the pristine catalyst, likely ascribed to the solid state counterion interactions (Figures S12-S14 in Supporting Information).

Further evidence has been acquired by means of XAS spectroscopy, which is emerging as a reference technique to dissect redox changes and evolution of the coordination sphere of competent WOCs.[39-42] In particular, this technique has been used to confirm the POM-based structural features for $[Co_4(H_2O)_2(PW_9O_{34})_2]^{10-}$, after oxygen evolution upon reaction with $Ru(bpy)_3^{3+}$.[39] The XANES spectra, at the Cobalt K-edge, are reported in Figure 5 for the pristine Co-POMs (crystalline powders, black traces), for their solid state ionic adducts with $Ru(bpy)_3^{2+}$ (blue traces) and for the spent reaction solutions (total [Co] = 147 μM, in 20 mM phosphate buffer, pH 8, red traces). The superimposed edge position of the $[Co^{II}(H_2O)_6](NO_3)_2$, used as a reference (black dotted trace in figure 5 top), that overlaps with that of the pristine Co-POMs as crystalline powder samples (black traces in figure 5), confirms the Co(II) oxidation state observed in the crystallographic structures of the polyanions.[39] Identical edges are recorded for the solid state adducts of the Co-POMs with $Ru(bpy)_3^{2+}$ (blue traces in figure 5) confirming the Co(II) oxidation state in the POM adduct and the innocent role of the photosentizer in its ground state interaction with the Co-POM catalysts. After photoirradiation and oxygen evolution, the spent reaction mixtures (red traces in figure 5) reveals an edge shift of the XANES spectrum that is consistent with a slight increase of the average oxidation state of Cobalt to about +2.2.[39] This observation has some important implications: (i) it rules out the structural leaching of Co(II) aqua ions;[39] (ii) it rules out the irreversible formation of Co^{III}-oxide colloids as competent WOC of the sacrificial cycle (compare with dashed line reference in Figure 5).[39,40]

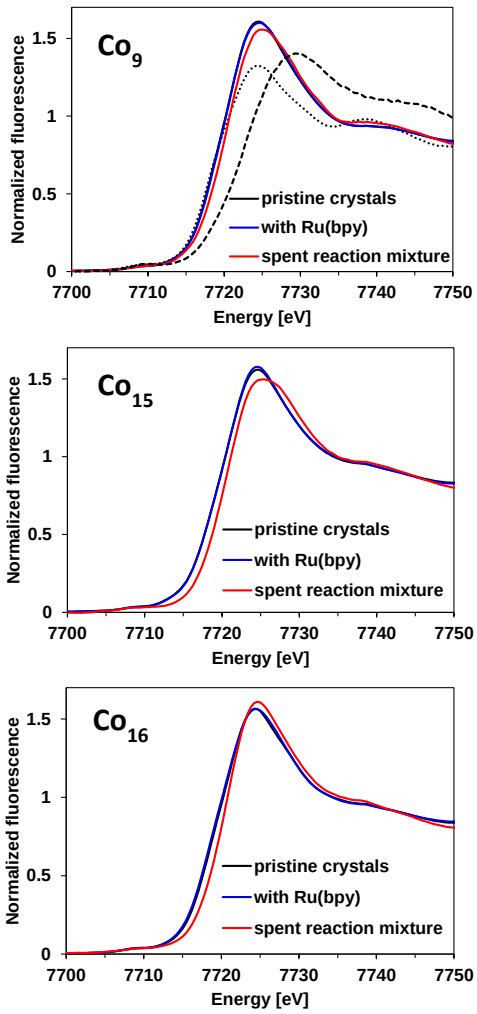

Figure 5. XANES spectra at the Cobalt K-edge. Black traces: pristine crystals of Co-POMs (solid samples); blue traces: adducts of Co-POMs with $Ru(bpy)_3^{2+}$ (solid samples); red traces: spent reaction mixtures (solution samples, [Co] = 147 μM in 20 mM phosphate buffer, pH 8). In the first panel $[Co^{II}(OH_2)_6](NO_3)_2$ and Co^{III}-oxide reference spectra are shown with dotted and dashed line respectively (both from Ref. 37).

While the XANES region is sensitive to oxidation state of the metal and to the geometry in its first coordination sphere, the EXAFS part may provide structural information on the higher coordination spheres.[39] Figure S15 in Supporting Information reports the Fourier Transformed EXAFS of the crystalline powders of the three Co-POMs (black traces) and of their respective solid state Co-POMs / $Ru(bpy)_3^{2+}$ adducts (blue traces). No significant differences are apparent for **Co_9** and **Co_{15}**, suggesting that the coordination geometry of the Co(II) sites remains unchanged. Indeed, the distances and coordination numbers obtained from the simulations fit very well to the crystal structure (Table S1 in Supporting Information). On the other hand, in the case of **Co_{16}** (figure S15 bottom) a slight variation between the EXAFS pattern of the crystalline powder (black trace) and of the **Co_{16}** adduct with $Ru(bpy)_3^{2+}$ (blue trace) is ascribed to the absence of Co-P distances in the latter case (the coordination number changes

from 1.5 in **Co_{16}** crystalline powder to 0.1 in the **Co_{16}** with $Ru(bpy)_3^{2+}$, figure S15 and table S1). This suggests the occurrence of water exchange equilibria, involving the phosphate anions of the **Co_{16}** core, once dissolved in solution.
Registration of the EXAFS part of the spectra for the three Co-POMs under photocatalytic conditions, is experimentally challenging due to the low Co concentration employed in photocatalytic tests. The EXAFS spectrum from the spent reaction mixture was recorded in a shorter k-range (k12) only for the **Co_{16}** species (figure 6, and figure S16 and table S2 in the Supporting Information), since the XANES spectrum of its adduct with $Ru(bpy)_3^{2+}$ reported above was already indicating some structural rearrangement.[¥] This spectrum (red trace in figure 6) indicates some structural changes mostly related to the decrease of the number of short Co-Co vectors observed in the XRD structure at 3.03 and 3.78 Å distances as well as a decrease of the number of Co-P vectors (table S2 in Supporting Information). These structural changes may be related to formation of open coordination sites available for substrate water binding. Our results show no indications for the formation of the previously reported catalytically active Co(III)-oxide phase (orange trace in figure 6 refers to Nocera's CoPi catalyst), as the 2.81 Å Co-Co distance characteristic for the CoPi catalyst[39-41] is absent (table S2 in the Supporting Information).

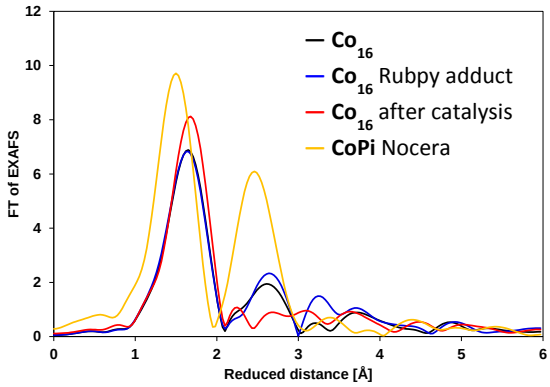

Figure 6. Fourier transform (10 – 600 eV above the edge) of EXAFS spectra at the Cobalt K-edge. Black trace: pristine crystals of **Co_{16}** (solid samples); blue trace: adducts of Co-POMs with $Ru(bpy)_3^{2+}$ (solid samples); red trace: spent reaction mixtures (solution samples, total Co concentration 147 μM in 20 mM phosphate buffer, pH 8); yellow trace: Nocera's Cobalt oxide/phosphate catalyst (CoPi).[38]

Conclusions

High nuclearity **Co_9**, **Co_{15}** and **Co_{16}** polyoxometalates have been investigated as earth-abundant WOCs in combination with $Ru(bpy)_3^{2+}/S_2O_8^{2-}$ under visible light irradiation. Converging kinetic and spectroscopic evidence is reported to show that:
- fast and multiple electron transfer occurs from the Co-POM to photogenerated $Ru(bpy)_3^{3+}$ with up to 32 ET events in 60 milliseconds, thus enabling the oxidation state climbing of the WOC manifold from Co(II) to Co(III) and Co(IV) states;
- the oxygen evolving kinetics are registered with no induction time, and a first order dependence on the Co-POM solution concentration;
- the WOC performance follows the trend **Co_{15}** ~ **Co_{16}** > **Co_9** in agreement with the flash photolysis results, indicating that fast multi-hole accumulation preludes to fast oxygen evolution under the conditions explored;
- the resident state of the Co-POMs after oxygenic turnover displays XANES spectra that are consistent with a photo-induced oxidation of the cobalt centres while retaining the POM features, thus ruling out structural leaching of Co(II) ions and evolution to cobalt oxide colloids.
As a corollary, in all cases the flash photolysis response of the Co-POMs under investigation is unique and diverse from Co(II) aqua ions and cobalt oxide materials, which is also apparent from the resulting quantum yield and molecular behaviour.
In particular **Co_{15}**, displaying a multi-nuclear cobalt cluster and satellite cobalt sites on the outer POM surface, has a prominent appeal vis-à-vis the high number of open coordination sites, that are accessible for water binding. Indeed, EXAFS studies confirm that **Co_{16}**, with no available coordination sites in its pristine state, undergoes phosphate exchange equilibria before entering the WOC regime. Besides the cobalt nuclearity, the availability of water molecules coordinated to Co(II) centers appears to be a mandatory feature to raise the cobalt oxidation state, likely involved in the oxygenic cycle. As far as the nature of the competent oxygenic intermediate is concerned, this is the less explored aspect in this field; while in recent years several reports were aimed at developing new catalysts with improved performance, the mechanistic requisites are still not fully understood.[43] This is however a crucial point in the design of durable photosynthetic assemblies, which need to be conceived to meet key sustainable constrains of process optimization. These include: (i) improvement of the cobalt WOC for high photo-efficiency using solar irradiation; (ii) design of a solid state device by immobilizing the catalyst on photo-electrodes; (iii) optimization of the WOC performance in a wide pH range that will leverage the modular assembly of an integrated water splitting device; (iv) WOC application in different aqueous media, and coupling with water remediation strategies.

Experimental

Synthesis of $[Co_9(H_2O)_6(OH)_3(PW_9O_{34})_3]^{16-}$ (**Co_9**),[25] $[Co_6(H_2O)_{30}\{Co_9Cl_2(OH)_3(H_2O)_9(SiW_8O_{31})_3\}]^{5-}$ (**Co_{15}**),[26a] and $[\{Co_4(OH)_3PO_4\}_4(PW_9O_{34})_4]^{16-}$ (**Co_{16}**)[27] was performed according to the published procedures.

Cyclic voltammetries were recorded on a BAS EC-epsilon labstation, with a glassy carbon (3 mm diameter) and a Pt wire as working and auxiliary electrodes, respectively. An Ag/AgCl (3 M NaCl) was used as the reference electrode.

UV-Vis absorption spectra were recorded on a UV/Vis/NIR Jasco V-570. Emission spectra were taken on a Horiba-Jobin

Yvon Fluoromax-2 spectrofluorimeter, equipped with a Hamamatsu R3896 tube. Infrared spectra were recorded on a Nicolet 5700 FT-IR spectrophotometer using KBr pellets.

Nanosecond transient measurements were performed with a custom laser spectrometer comprised of a Continuum Surelite II Nd:YAG laser (FWHM 6-8 ns) with frequency doubled, (532 nm, 330 mJ) or tripled, (355 nm, 160 mJ) option, an Applied Photophysics xenon light source including a mod. 720 150 W lamp housing, a mod. 620 power controlled lamp supply and a mod. 03-102 arc lamp pulser. Laser excitation was provided at 90° with respect to the white light probe beam. Light transmitted by the sample was focused onto the entrance slit of a 300 mm focal length Acton SpectraPro 2300i triple grating, flat field, double exit monochromator equipped with a photomultiplier detector (Hamamatsu R3896) and a Princeton Instruments PIMAX II gated intensified CCD camera, using a RB Gen II intensifier, a ST133 controller and a PTG pulser. Signals from the photomultiplier (kinetic traces) were processed by means of a LeCroy 9360 (600 MHz, 5 Gs/s) digital oscilloscope.

Photocatalyitic water oxidation tests were conducted in duplicates, in a custom-made glass reactor (solution volume = 15 mL) equipped with a steel cap, where a FOXY-R-AF probe was mounted and interfaced with a Neofox Real-Time software for data collection. Illumination was performed with a tungsten lamp at 150 W, with a 375 nm filter (illumination spot of 1 cm diameter, power density of 90 $mWcm^{-2}$). For quantum efficiency determination, irradiation was performed with a monochromatic LED (7 mW power) emitting at 450 nm; the photon flux was 2.63×10^{-8} einstein/s.

X-ray absorption spectroscopy (XAS): X-ray absorption data were collected at the KMC1 beamline at the BESSY II synchrotron (Helmholtz-Zentrum Berlin, Germany) at 20 K in a liquid-helium cryostat as described previously.[44] Data were collected in fluorescence mode using 13-element energy resolving Ge detector (Canberra) selecting the Mn K_α fluorescence line. 10 μm Co foil was measured simultaneously in absorption mode for energy calibration (first inflection point of the Co edge was set to 7709 eV). For the extraction of EXAFS data (conversion to *k*-space) E_0 = 7710 eV was used. Other details about data analysis and simulations are provided in reference 44.

Acknowledgements

Financial support from Fondazione Cariparo (Starting Grant) and from Italo-Israelian Scientific & Technological Cooperation project "SOGNO", COST actions CM1203 Polyoxometalate Chemistry for Molecular Nanoscience (PoCheMoN), CM1202 ''PERSPECT-H2O'' and CM1205 "CARISMA: CAtalytic RoutInes for Small Molecule Activation" are gratefully acknowledged. This work was also partially funded by the Spanish Ministerio de Economía y Competitividad (MINECO) through project CTQ2015-71287-R and the Severo Ochoa Excellence Accreditation (2014-2018) SEV-2013-0319; and by the Generalitat de Catalunya (CERCA Programme and 2014 SGR-797). UK acknowledges German Science Foundation (DFG), German Academic Exchange Council (DAAD), and Jacobs University for financial support. HD and IZ acknowledge financial support from the Berlin Cluster of Excellence on Unifying Concepts in Catalysis (UniCat, EXL 31411).

Notes and references

‡ These six $Co(H_2O)_5$ groups, although linked by a single oxygen bridge to the POM cage and therefore possibly susceptible to detachment from it, play an important role in stabilizing the structure, by reducing the overall negative charge of the polyanion and it was demonstrated that these external cobalt ions are not labile in solution.[25a]

§ Alternatively, this core was described as a central $\{Co_4O_4\}$ cubane unit, where oxygen atoms are shared with four phosphate groups, and capped by four tri-cobalt(II) $\{Co(\mu_2\text{-}OH)\}_3$ units.

‡‡ Broadening of the ^{31}P NMR signal relative to the phosphate buffer may also arise from paramagnetic Co-POMs.

§§ Typically, primary formation of $[Ru(bpy)_3]^{3+}$ (eqn (1) and (2)) takes place within the time resolution of the experiment (10 ns) while the secondary formation by reaction with the sulfate radical (eqn (3)) in ca. 5 μs.

‖ In the case of **Co_9** the anodic process associated to the Co(III)/Co(II) redox couple occurs at potentials close to the catalytic water oxidation discharge and it is not detected by square-wave voltammetry (SWV), see ref. 19a. Electrochemical analysis of the Co-POMs in non aqueous medium (i.e. CH_3CN) is generally performed by counterion methatesis with tetra-alkylammonium salts that may affect the POM stability in organic solvents. Moreover, non-aqueous media rule out the access to proton coupled electron transfer events that are key features for water oxidation mechanism by cobalt catalysts.

¶ ET in a μs time domain were observed for a Co-POM with an embedded $Co(II)(H_2O)$ moiety.

♣ This analysis is aimed at revealing possible rearrangement of POM based species; however, the possibility that some species derived from the Co-POMs may be not precipitated from the reaction mixture could be considered.

¥ **Co_{16}** type polyanions were previously reported to be stable under oxygen evolving conditions combined with $Ru(bpy)_3^{2+}/S_2O_8^{2-}$ (see ref. 20b); this apparent discrepancy with the present work could be likely associated to the different reaction conditions employed in ref. 20b (80 mM borate buffer, pH 9).

1 K. S. Joya, Y. F. Joya, K. Ocakoglu, R. van de Krol, *Angew. Chem., Int. Ed.* 2013, **52**, 10426.
2 (a) M. D. Kärkäs, O. Verho, E. V. Johnston, B. Åkermark, *Chem. Rev.* 2014, **114**, 11863. (b) J. R. Galán-Mascarós, *ChemElectroChem* 2015, **2**, 37.
3 (a) N. Cox, M. Retegan, F. Neese, D. A. Pantazis, A. Boussac, W. Lubitz, *Science* 2014, **345**, 804. (b) J. Yano, V. Yachandra, *Chem. Rev.* 2014, **114**, 4175. (c) M. Suga, F. Akita, K. Hirata, G. Ueno, H. Murakami, Y. Nakajima, T. Shimizu, K. Yamashita, M. Yamamoto, H. Ago, J.-R. Shen, *Nature* 2015, **517**, 99.
4 Themed collection on Polyoxometalate cluster science, L. Cronin and A. Müller guest editors, *Chem. Soc. Rev.* 2012, **22**, 7325–7648.
5 A. Sartorel, M. Bonchio, S. Campagna, F. Scandola, *Chem. Soc. Rev.*, 2013, **42**, 2262.

6 (a) H. Lv, Y. V. Geletii, C. Zhao, J. W. Vickers, G. Zhu, Z. Luo, J. Song, T. Lian, D. G. Musaev, C. L. Hill, *Chem. Soc. Rev.* 2012, **41**, 7572. (b) G. Geisberger, S. Paulus, M. Carraro, M. Bonchio, G. R. Patzke, *Chem. Eur. J.* 2011, **17**, 4619.

7 (a) M. Quintana, A. M. López, S. Rapino, F. M. Toma, M. Iurlo, M. Carraro, A. Sartorel, C. Maccato, X. Ke, C. Bittencourt, T. Da Ros, G. Van Tendeloo, M. Marcaccio, F. Paolucci, M. Prato, M. Bonchio, *ACS Nano* 2013, **7**, 811. (b) F. M. Toma, A. Sartorel, M. Iurlo, M. Carraro, P. Parisse, C. Maccato, S. Rapino, B. Rodriguez Gonzalez, H. Amenitsch, T. Da Ros, L. Casalis, A. Goldoni, M. Marcaccio, G. Scorrano, G. Scoles, F. Paolucci, M. Prato and M. Bonchio, *Nat. Chem.* 2010, **2**, 826.

8 M. W. Kanan, Y. Surendranath, D. G. Nocera, *Chem. Soc. Rev*. 2008, **321**, 109.

9 (a) J. B. Gerken, J. G. McAlpin, J. Y. C. Chen, M. L. Rigsby, W. H. Casey, R. D. Britt, S. S. Stahl, *J. Am. Chem. Soc.* 2012, **133**, 14431. (b) F. Jiao, H. Frei, *Angew. Chem., Int. Ed.*, 2009, **48**, 1841. (c) J. Rosen, G. S. Hutchings, F. Jiao, *J. Am. Chem. Soc.* 2013, **135**, 4516. (d) S. Yusuf, F. Jiao, *ACS Catal.* 2012, **2**, 2753. (e) N. Shi, W. Cheng, H. Zhou, T. Fan, M. Niederberger, *Chem. Commun.* 2015, **51**, 1338. (f) M. Grzelczak, J. Zhang, J. Pfrommer, J. Hartmann, M. Driess, M. Antonietti, X. Wang *ACS Catal.* 2013, **3**, 383. (g) G. S. Hutchings, Y. Zhang, J. Li, B. T. Yonemoto, X. Zhou, K. Zhu, F. Jiao *J. Am. Chem. Soc.* 2015, **137**, 4223. (h) X. Deng, W. N. Schmidt, H. Tüysüz *Chem. Mater.* 2014, **26**, 6127. (i) X. Deng, H. Tüysüz *ACS Catal.* 2014, **4**, 3701. (j) J. D. Blakemore, H. B. Gray, J. R. Winkler, A. M. Müller *ACS Catal.* 2013, **3**, 2497. (h) S. Du, Z. Ren, Y. Qu, J. Wu, W. Xi, J. Zhu, H. Fu, *Chem. Commun.* **2016**, *52*, 6705.

10 S. Tanaka, M. Annaka, K. Sakai, *Chem. Commun.* 2012, **48**, 1653.

11 F. Song, Y. Ding, B. Ma, C. Wang, Q. Wang, X. Du, S. Fua, J. Song, *Energy Environ. Sci.* 2013, **6**, 1170.

12 Q. Yin, J. M. Tan, C. Besson, Y. V. Geletii, D. G. Musaev, A. E. Kuznetsov, Z. Luo, K. I. Hardcastle, C. L. Hill, *Science*, 2010, **328**, 342.

13 (a) J. J. Stracke, R. G. Finke, *J. Am. Chem. Soc.* 2011, **133**, 14872. (b) J. J. Stracke, R. G. Finke, *ACS Catal.* 2013, **3**, 1209. (c) J. J. Stracke, R. G. Finke, *ACS Catal.* 2014, **4**, 79. (d) J. J. Stracke, R. G. Finke, *ACS Catal.* 2014, **4**, 909. (e) S. J. Folkman, R. G. Finke, *ACS Catal.* 2017, **7**, 7.

14 M. Natali, S. Berardi, A. Sartorel, M. Bonchio, S. Campagna, F. Scandola, *Chem. Commun.* 2012, **48**, 8808.

15 (a) J. W. Vickers, H. Lv, J. M. Sumliner, G. Zhu, Z. Luo, D. G. Musaev, Y. V. Geletii, C. L. Hill, *J. Am. Chem. Soc.* 2013, **135**, 14110. (b) Z. Huang, Z. Luo, Y. V. Geletii, J. W. Vickers, Q. Yin, D. Wu, Y. Hou, Y. Ding, J. Song, D. G. Musaev, C. L. Hill, T. Lian, *J. Am. Chem. Soc.* 2011, **133**, 2068.

16 H. Lv, J. Song, Y. V. Geletii, J. W. Vickers, J. M. Sumliner, D. G. Musaev, P. Kögerler, P. F. Zhuk, J. Bacsa, G. Zhu, C. L. Hill, *J. Am. Chem. Soc.* 2014, **136**, 9268.

17 G. Zhu, Y. V. Geletii, P. Kögerler, H. Schilder, J. Song, S. Lense, C. Zhao, K. I. Hardcastle, D. G. Musaev, C. L. Hill, *Dalton Trans.* 2012, **41**, 2084.

18 P.-E. Car, M. Guttentag, K. K. Baldridge, R. Alberto, G. R. Patzke, *Green Chem.* 2012, **14**, 1680.

19 (a) S. Goberna-Ferron, L. Vigara, J. Soriano-López, J. R. Galán-Mascarós, *Inorg. Chem.* 2012, **51**, 11707. (b) S. Goberna-Ferron, J. Soriano-López, J. R. Galán-Mascarós, M. Nyman, *Eur. J. Inorg. Chem.* 2015, 2833.

20 (a) R. Al-Oweini, B. S. Bassil, J. Friedl, V. Kottisch, M. Ibrahim, M. Asano, B. Keita, G. Novitchi, Y. Lan, A. Powell, U. Stimming, U. Kortz, *Inorg. Chem.* 2014, **53**, 5663. (b) X.-B. Han, Z.-M. Zhang, T. Zhang, Y.-G. Li, W. Lin, W. You, Z.-M. Su, E.-B. Wang, *J. Am. Chem. Soc.* 2014, **136**, 5359.

21 J. Soriano-López, S. Goberna-Ferron, L. Vigara, J. J. Carbó, J. M. Poblet, J. R. Galán-Mascarós, *Inorg. Chem.* 2013, **52**, 4753.

22 (a) M. Orlandi, R. Argazzi, A. Sartorel, M. Carraro, G. Scorrano, M. Bonchio, F. Scandola, *Chem. Commun.* 2010, **46**, 3152. (b) M. Natali, M. Orlandi, S. Berardi, S. Campagna, M. Bonchio, A. Sartorel, F. Scandola, *Inorg. Chem*., 2012, **51**, 7324.

23 M. Natali, F. Puntoriero, C. Chiorboli, G. La Ganga, A. Sartorel, M. Bonchio, S. Campagna, F. Scandola, *J. Phys. Chem. C* 2015, **119**, 2371.

24 R. Al-Oweini, A. Sartorel, B. S. Bassil, M. Natali, S. Berardi, F. Scandola, U. Kortz, M. Bonchio, *Angew. Chem. Int. Ed.* 2014, **53**, 11182.

25 J. R. Galán-Mascarós, C. J. Gómez-García, J. J. Borrás-Almenar, E. Coronado, *Adv. Mater.* 1994, **6**, 221.

26 (a) B. S. Bassil, S. Nellutla, U. Kortz, A. C. Stowe, J. van Tol, N. S. Dalal, B. Keita, L. Nadjo, *Inorg. Chem.* 2005, **44**, 2659. (b) B. Keita, U. Kortz, L. R. Brudna Holzle, S. Brown, L. Nadjo, *Langmuir* 2007, **23**, 9531.

27 M. Ibrahim, Y. Lan, B. S. Bassil, Y. Xiang, A. Suchopar, A. K. Powell, U. Kortz, *Angew. Chem. Int. Ed.* 2011, **50**, 4708.

28 (a) A. Montellano López, M. Natali, E. Pizzolato, C. Chiorboli, M. Bonchio, A. Sartorel, F. Scandola, *Phys. Chem. Chem. Phys.* 2014, **16**, 12000. (b) E. Pizzolato, M. Natali, B. Posocco, A. Montellano López, I. Bazzan, M. Di Valentin, P. Galloni, V. Conte, M. Bonchio, F. Scandola, A. Sartorel *Chem. Commun.* 2013, **49**, 9941. (c) F. Li, Y. Jiang, B. Zhang, F. Huang, Y. Gao, L. Sun, *Angew. Chem., Int. Ed.* 2012, **51**, 2417.

29 C. P. Plaisance, R. A. Van Santen, *J. Am. Chem. Soc.* 2015, **137**, 14660.

30 (a) M. Zhang, H. Frei *Catal. Lett.* 2015, **145**, 420. (b) M. Zhang, M. de Respinis, H. Frei *Nat. Chem.* 2014, **6**, 362. (c) T. Ling, D.-Y. Yan, H. Wang, Y. Zheng, X. Zheng, J. Mao, X.-W. Du, Z. Hu, M. Jaroniec, S.-Z. Qiao, *Nat. Commun.* 2016, **7**, article number: 12876. (d) H.-Y. Wang, S.-F. Huang, H.-Y. Chen, T.-S. Chan, H. M. Chen, B. Liu, *J. Am. Chem. Soc.* 2016, **138**, 36.

31 A. M. Ullman, Y. Liu, M. Huynh, D. K. Bediako, H. Wang, B. L. Anderson, D. C. Powers, J. J. Breen, H. D. Abruña and D. G. Nocera, *J. Am. Chem. Soc.*, 2014, **136**, 17681.

32 M. Natali, E. Deponti, D. Vilona, A. Sartorel, M. Bonchio, F. Scandola, *Eur. J. Inorg. Chem.* 2015, 3467.

33 I. A. Weinstock, *Chem. Rev.* 1998, **98**, 113.

34 H. S. White, W. G. Becker, A. J. Bard, *J. Phys. Chem.* 1984, **88**, 1840.

35 (a) N. D. Morris, M. Suzuki, T. E. Mallouk, *J. Phys. Chem. A* 2004, **108**, 9115. (b) W. J. Youngblood, S.-H. A. Lee, Y. Kobayashi, E. A. Hernandez-Pagan, P. G. Hoertz, T. A. Moore, A. L. Moore, D. Gust, T. E. Mallouk, *J. Am. Chem. Soc.* 2009, **131**, 926.

36 D. R. Weinberg, C. J. Gagliardi, J. F. Hull, C. F. Murphy, C. A. Kent, B. C. Westlake, A. Paul, D. H. Ess, D. G. McCafferty, T. J. Meyer, *Chem. Rev.* 2012, **112**, 4016.

37 Y. Surendranath, M. W. Kanan, D. G. Nocera, *J. Am. Chem. Soc.* 2010, **132**, 16501.

38 A. Genoni, G. La Ganga, A. Volpe, F. Puntoriero, M. Di Valentin, M. Bonchio, M. Natali, A. Sartorel, *Faraday Disc.* 2015, **185**, 121.

39 R. Schiwon, K. Klingan, H. Dau, C. Limberg, *Chem. Commun.* 2014, **50**, 100.

40 (a) M. Risch, V. Khare, I. Zaharieva, L. Gerencser, P. Chernev, H. Dau, *J. Am. Chem. Soc.* 2009, **131,** 6936. (b) M. Risch, F. Ringleb, M. Kohlhoff, P. Bogdanoff, P. Chernev, I. Zaharieva, H. Dau, *En. Env. Sci.* 2015, **8**, 661.

41 M. W. Kanan, J. Yano, Y. Surendranath, M. DInca, V. K. Yachandra, D. G. Nocera, *J. Am. Chem. Soc.* 2010, **132**, 13692.
42 S. Piccinin, A. Sartorel, G. Aquilanti, A. Goldoni, M. Bonchio, S. Fabris, *Proc. Natl. Acad. Sci. U. S. A.*, 2013, **110**, 4917.
43 X. Sala, S. Maji, R. Bofill, J. García-Antón, L. Escriche, A. Llobet, *Acc. Chem. Res.* 2014, **47**, 504.
44 M. Wiechen, I. Zaharieva, H. Dau, P. Kurz, *Chem. Sci*. 2012, **3**, 2330.